ORIGINAL PAPER

Robust mixed FE for analyses of higher-order electromechanical coupling in piezoelectric solids

Prince Henry Serrao[1] · Sergey Kozinov[1]

Abstract

Direct flexoelectricity is a size-dependent phenomenon, very prominent at smaller scales, that connects the strain gradients and the electric field. The very existence of strain gradients enhances noncentrosymmetry and heightens the interaction between piezoelectricity and flexoelectricity, demanding fully coupled higher-order electromechanical formulations. The numerical instability of the existing finite elements used to model flexoelectricity alone is revealed due to their reliance on the stabilization parameter. Thus, two new finite elements `Qu2s2p2l0` (`QL0-4`) and `Qu2s2p2l1` (`QL1-16`) are proposed for mixed FEM that are numerically robust without any need of such stabilization parameters. Additionally, the existing finite element `Qu2s1p2l0` [`Q47` in (Deng et al. in J Appl Mech 84:081004, 2017)], is implemented from scratch to replicate known results and benchmark the performance of newly proposed finite elements. To verify the robustness of these elements, various benchmark problems for flexoelectricity in dielectric solids, such as a thick cylinder and truncated pyramid are simulated. The great agreement of the numerical results with the existing ones reflects the foundational nature of the proposed elements. Furthermore, the proposed mixed finite elements were used to successfully analyze cantilever beam and truncated pyramid problems where piezoelectric effects were taken into account for the first time. Current results are intrumental in simulating flexoelectricity and piezoelectricity together to highlight their interactions using newly proposed numerically robust finite elements.

Keywords Flexoelectricity · Higher-order electromechanical theory · Numerically robust mixed FE · Fully coupled electromechanical framework · Flexoelectricity extended with piezoelectric contribution

1 Introduction

Piezoelectricity was discovered in 1880 [2]. According to this phenomenon, mechanical energy could be converted to electrical energy and vice versa, known as two-way linear electromechanical coupling. Direct piezoelectricity is defined as the generation of electrical voltage across the (poly)crystal on the application of mechanical strains. In contrast, converse piezoelectricity causes mechanical distortion on the application of electrical voltage difference. However, piezoelectricity is only observed in dielectrics without centrosymmetry. This is a limitation of the choice of dielectric material for the application of piezoelectricity in microelectromechanical systems (MEMS). As a universal alternative,

flexoelectricity is the most advanced phenomenon observed in all dielectrics. Flexoelectricity is the coupling between strain gradients and electric field or electric field gradient and mechanical strains [3]. Flexoelectricity was first put forth more than 60 years ago [4]; however, it was only quantified a decade later for the first time [5]. It has regained attention because of the experimental evidence obtained of flexoelectricity due to technological advances [6–8]. Also, flexoelectricity involves mechanical strain gradients. As gradients are inversely proportional to the length scale on which they are applied, i.e., a size-dependent effect, flexoelectricity is very prominent at smaller scales such as micrometer- or nanometer-scales [9]. This illustrates promising applications of flexoelectricity along with non-linear material behavior of ferroelectricity for high-precision devices in MEMS [10–12].

Classical continuum theory cannot capture the length scale effect due to the absence of material length scale parameter in the formulations. Material length scales were introduced by Cosserat [13] due to strain gradients and were significantly

✉ Sergey Kozinov
sergey.kozinov@rub.de

[1] Chair of Continuum Mechanics, Ruhr University Bochum, Universitätsstraße 150, Bochum 44801, Germany

extended and improved in [14, 15]. Such gradient-based theories lead to fourth-order partial differential equations dependent on displacements that demand C^1-continuous elements for the standard finite element method (FEM) to be used. Since then, various methods such as meshfree methods, iso-geometric analysis, C^1-continuous elements, mixed FEM (MFEM), have been developed to solve problems involving gradients [16].

The meshfree method was initially proposed for flexoelectricity based on local maximum entropy [3]. Using this method, different boundary value problems (BVP) based on the experimental setup given in [17–19] were simulated. However, the meshfree method is still in its embryonic stage and is under development [16]. Iso-geometric analysis (IGA) is a new method first proposed in [20]. This technique uses nonuniform rational B-splines (NURBS), which could be of any arbitrary order based on the definition of its basis function [21]. This enables IGA to be applied to complex problems where gradients can be incorporated easily. This being said, IGA is also used for modeling flexoelectricity [22–24]. Nevertheless, similar to the meshfree method, IGA also has some prominent drawbacks, such as gaps and overlaps that needs to be accounted for [25]. Another technique directly utilizes C^1-continuous elements, such as those proposed in [26]. However, such elements are complicated in their implementation due to the use of higher-order basis functions and involve higher complexities and computational costs in 3D. Immersed boundary method based on a hierarchical B-Spline inspired by IGA for flexoelectricity is proposed in [27]. In the immediate past, a collocation-based mixed finite element for flexoelectricity was proposed in [28, 29]. Recently, the authors proposed a second-order collocation based mixed finite element that is capable of capturing flexoelectricity more precisely [30]. It was demonstrated that it is challenging to enforce C^1-continuity even in a weak sense with collocation-based formulations, and the need for a smoothing scheme is inevitable. Further, the authors also developed a 3D collocation-based mixed finite element to eradicate the computational expensiveness of the traditional mixed FEM [31].

MFEM is a prominent method already employed and tested for flexoelectricity [1, 32–34]. This technique assumes mechanical displacements and their gradients as independent variables. The compatibility between the mechanical strains (computed based on mechanical displacements) and independently assumed strains as kinematic constraints are enforced using Lagrange multipliers [35, 36]. It is experimentally challenging to separate flexoelectricity and piezoelectricity [11]. Applying a mechanical strain gradient breaks the centrosymmetry of the unit cell which activates flexoelectricity. In case of noncentrosymmetric crystalline structure, such mechanical strain gradient either enhances or suppresses existing piezoelectric coupling. Hence, fully coupled higher-order

electromechanical formulations are necessary. Most of the available literatures based on MFEM has considered only flexoelectricity in centrosymmetric dielectrics and neglected piezoelectric impact [1, 32–34].

In this work, fully coupled electromechanical formulations for flexoelectricity in dielectric and piezoelectric solids are presented. MFEM is utilized to model flexoelectricity with weakly enforced C^1-continuous behavior. Lagrange multipliers enforce kinematic constraints analogously to [35, 36]. In Sect. 2, constitutive and governing equations and necessary boundary conditions for flexoelectricity and piezoelectricity are described. In Sect. 3, variational formulations of mixed FEM for deriving weak form are given. In Sect. 4, mixed finite element implementation along with three different types of user element that includes two newly proposed user elements are presented. In Sect. 5, the user elements implemented in Fortran are exclusively verified for linear and higher-order electromechanical theories using BVPs from various literature. Thereafter, a piezoelectric truncated pyramid with flexoelectric effect is calculated for the first time. In Sect. 5.5, the newly proposed elements are compared with the known user element [1] based on the influence of stabilization parameter on results. Finally, in Sect. 6, the key conclusions from this work are summarized.

2 Higher-order electromechanical theory in piezoelectric solids

2.1 Strain gradient elasticity theory

Current subsection summarizes the classical strain gradient elasticity (SGE) theory in brief.

A fixed rectangular Cartesian system with orthonormal base vectors e_i ($i = 1, 2, 3$) is assumed. Einstein summation convention is used for repeated (dummy) indices. For small deformations, mechanical strains can be defined from the mechanical displacements u_i as

$$\varepsilon_{ij} = \frac{1}{2}\left[u_{i,j} + u_{j,i}\right],\tag{1}$$

where $()_{,j}$ represents the partial derivative of the field with respect to x_j. Rotation gradient χ_{ij} and rotation vector θ_i are defined as [36]:

$$\chi_{ij} = \theta_{j,i}, \qquad \theta_i = \frac{1}{2}\epsilon_{ijk}u_{k,j},\tag{2}$$

where ϵ_{ijk} is the Levi-Civita permutation tensor. In [15], three different forms of strain gradient elasticity theory based on

the different definitions of strain gradients were proposed as

$$
\tilde{\eta}_{ijk} = u_{k,ij}, \quad \hat{\eta}_{ijk} = \frac{1}{2}\left[u_{j,ki} + u_{k,ij}\right],
$$
$$
\bar{\bar{\eta}}_{ijk} = \frac{1}{3}\left[u_{i,jk} + u_{j,ki} + u_{k,ij}\right].
\tag{3}
$$

In [36], different forms of SGE theories for general strain gradient solids given in [15] are analyzed in detail, and three forms of internal energy density are presented:

$$
\mathcal{U} = \tilde{\mathcal{U}}(\varepsilon_{ij}, \tilde{\eta}_{ijk}) = \hat{\mathcal{U}}(\varepsilon_{ij}, \hat{\eta}_{ijk}) = \bar{\bar{\mathcal{U}}}(\varepsilon_{ij}, \chi_{ij}, \bar{\bar{\eta}}_{ijk}),
\tag{4}
$$

where specifically,

$$
\tilde{\mathcal{U}} = \frac{1}{2}\lambda\varepsilon_{ii}\varepsilon_{jj} + \mu\varepsilon_{ij}\varepsilon_{ij}
$$
$$
+ \frac{1}{2}l^2\left[\lambda\tilde{\eta}_{ijj}\tilde{\eta}_{ikk} + \mu\left[\tilde{\eta}_{ijk}\tilde{\eta}_{ijk} + \tilde{\eta}_{ijk}\tilde{\eta}_{kji}\right]\right],
\tag{5a}
$$
$$
\hat{\mathcal{U}} = \frac{1}{2}\lambda\varepsilon_{ii}\varepsilon_{jj} + \mu\varepsilon_{ij}\varepsilon_{ij} + \frac{1}{2}l^2\left[\lambda\hat{\eta}_{ijj}\hat{\eta}_{ikk} + 2\mu\hat{\eta}_{ijk}\hat{\eta}_{ijk}\right],
\tag{5b}
$$
$$
\bar{\bar{\mathcal{U}}} = \frac{1}{2}\lambda\varepsilon_{ii}\varepsilon_{jj} + \mu\varepsilon_{ij}\varepsilon_{ij} + l^2\left[\frac{2}{9}\left[\lambda + 3\mu\right]\chi_{ij}\chi_{ij} - \frac{2}{9}\lambda\chi_{ij}\chi_{ji}\right.
$$
$$
\left. + \frac{1}{2}\lambda\bar{\bar{\eta}}_{iij}\bar{\bar{\eta}}_{kkj} + \mu\bar{\bar{\eta}}_{ijk}\bar{\bar{\eta}}_{ijk} + \frac{2}{3}\lambda\epsilon_{ijk}\chi_{ij}\bar{\bar{\eta}}_{kpp}\right].
\tag{5c}
$$

In the present work, both type I and type II forms given in Eqs. (5a) and (5b) were implemented and evaluated. Since type II is an equivalent of type I form [36], the numerical examples, as expected, yielded identical results using type II equations as those with type I equations. Therefore, only the details pertaining to the type I form are included hereon. It is observed that the above-described forms perform well for a wide range of problems such as thick cylinder [1], plate with a hole under biaxial loading [36], cantilever beam in open and closed circuit condition [16].

2.2 Constitutive equations for flexoelectricity including piezoelectricity

SGE formulations are now extended with higher-order electromechanical coupling between the strain gradients and electric field to encompass flexoelectricity. Beyond that, the linear electromechanical coupling is considered for the fully coupled numerical simulations of size-dependent piezoelectric structures. Most authors have modeled flexoelectricity neglecting piezoelectric contribution [1, 3, 28, 32] due to simulation simplicity which includes the isotropic mechanical and dielectric tensors assumption while neglecting the anisotropic piezoelectric material tensor.

The general form of internal energy density based on electric polarization is presented in [37]. Since it is relatively easier to work with the alternative equivalent form based on an electric field, the electric enthalpy density obtained

after the Legendre transformation is considered as a function of the electric field [1, 3, 16, 28]. Based on the SGE theory that involves the first gradient of mechanical strains, the general form of electric enthalpy density for direct flexoelectricity obtained by permutation of all mechanical and electrical terms is given as

$$
\tilde{h}(\varepsilon_{ij}, \tilde{\eta}_{ijk}, E_i) = \frac{1}{2}\mathcal{C}_{ijkl}\varepsilon_{ij}\varepsilon_{kl} + \frac{1}{2}\mathcal{A}_{ijklmn}\tilde{\eta}_{ijk}\tilde{\eta}_{lmn}
$$
$$
- \frac{1}{2}\kappa_{ij}E_iE_j - d_{kij}E_k\varepsilon_{ij} - f_{ijkl}E_i\tilde{\eta}_{jkl}.
\tag{6}
$$

where E_i is the electric field that relates to electric potential ϕ as $E_i = -\phi_{,i}$, $\mathcal{C}_{ijkl}$ is elastic stiffness tensor, $\mathcal{A}_{ijklmn}$ is the higher order elasticity tensor from SGE theory. κ_{ij} is dielectric permittivity tensor. d_{ijk} is piezoelectric tensor whereas f_{ijkl} is direct flexoelectric tensor.

The constitutive equations for the thermodynamic conjugates which are mechanical stress σ_{ij}, higher order stress τ_{ijk} and electric displacement $\mathcal{D}_i^e$ for the mechanical strain ε_{ij}, type I strain gradient $\tilde{\eta}_{ijk}$ and electric field E_i, respectively are

$$
\sigma_{ij} = \frac{\partial\tilde{h}}{\partial\varepsilon_{ij}} = \mathcal{C}_{ijkl}\varepsilon_{kl} - d_{kij}E_k,
\tag{7a}
$$
$$
\tau_{jkl} = \frac{\partial\tilde{h}}{\partial\tilde{\eta}_{jkl}} = \mathcal{A}_{jklmni}\tilde{\eta}_{mni} - f_{ijkl}E_i,
\tag{7b}
$$
$$
\mathcal{D}_i^e = -\frac{\partial\tilde{h}}{\partial E_i} = \kappa_{ij}E_j + d_{ijk}\varepsilon_{jk} + f_{ijkl}\tilde{\eta}_{jkl}.
\tag{7c}
$$

Piezoelectricity influences mechanical stress but has no direct contribution to higher-order stress. Further based on Eq. (7b), flexoelectricity influences higher-order stress but has no direct involvement in mechanical stress. However, the interconnection between the higher-order stress and the mechanical stress is evident from the natural boundary condition given in Eq. (12), that needs to satisfied. However, both of these phenomena explicitly influence electric displacement.

2.3 Balance equations and boundary conditions for flexoelectricity

The balance equations and boundary conditions are derived following [37, 38]. The momentum equilibrium and maxwell equations for a bulk body with volume $\mathcal{V}$ and surface A, in which volumetric body forces b_i and volumetric free charges q^e are acting, have the form

$$
\sigma_{ij,j} - \tau_{ijk,kj} + b_i = 0,
\tag{8a}
$$
$$
\mathcal{D}_{i,i}^e + q^e = 0.
\tag{8b}
$$

For a complete description of the problem, the associated essential and natural boundary conditions are described below.

1. Essential (Dirichlet) boundary conditions:

    (a) Prescribed displacement on mechanical displacement boundary $\partial \mathcal{V}_u$

    $$u_i = \bar{u}_i \tag{9}$$

    (b) Prescribed electric potential on electric potential boundary $\partial \mathcal{V}_\phi$

    $$\phi = \bar{\phi} \tag{10}$$

    (c) Prescribed normal derivative of mechanical displacement on the corresponding boundary $\partial \mathcal{V}_{u,n}$

    $$\nabla_{\mathbf{n}} u_i = u_{i,l} n_l = \bar{u}_{i,l} n_l \tag{11}$$

2. Natural (Neumann) boundary conditions:

    (a) Prescribed tractions on traction boundary $\partial \mathcal{V}_t$ with $\partial \mathcal{V}_u \cup \partial \mathcal{V}_t = \partial \mathcal{V}, \partial \mathcal{V}_u \cap \partial \mathcal{V}_t = \emptyset$

    $$\begin{aligned} & \left[\sigma_{ij} - \tau_{ijk,k} \right] n_j + \left[D_l^t (n_l) \right] \tau_{ijm} n_j n_m \\ & - D_j^t \left(\tau_{ijm} n_m \right) = \bar{t}_i \end{aligned} \tag{12}$$

    (b) Prescribed surface charges on boundary $\partial \mathcal{V}_\omega$ with $\partial \mathcal{V}_\phi \cup \partial \mathcal{V}_\omega = \partial \mathcal{V}, \partial \mathcal{V}_\phi \cap \partial \mathcal{V}_\omega = \emptyset$

    $$\mathcal{D}_i^e n_i = \bar{\omega} \tag{13}$$

    (c) Prescribed higher order traction on corresponding boundary $\partial \mathcal{V}_\tau$ with $\partial \mathcal{V}_{u,n} \cup \partial \mathcal{V}_\tau = \partial \mathcal{V}, \partial \mathcal{V}_{u,n} \cap \partial \mathcal{V}_\tau = \emptyset$

    $$\tau_{ijm} n_m n_j = \bar{\tau}_i \tag{14}$$

    (d) Jump $[\![\bullet]\!]$, indicates the difference in the enclosed quantity across edges c^α formed by intersection of smooth surfaces. Closed curves bound the smooth surfaces (in a counter-clockwise direction) in which s_i is the unit vector tangent to c^α and $\mathbf{m} = \mathbf{s} \times \mathbf{n}$.

    $$[\![m_j \tau_{ijk} n_k]\!] = \bar{T} \tag{15}$$

The boundary condition Eq. (11) is active due to the SGE theory, whereas boundary condition Eq. (13) is active due to flexoelectricity.

3 Variational principle with kinematic constraints

The equivalent form of electric enthalpy density of the system given in Eq. (6) based on constitutive Eqs. (7) can be written as

$$\tilde{h}(\varepsilon_{ij}, \tilde{\eta}_{ijk}, E_i) = \frac{1}{2} \sigma_{ij} \varepsilon_{ij} + \frac{1}{2} \tau_{ijm} \tilde{\eta}_{ijm} + \frac{1}{2} \mathcal{D}_i^e E_i. \tag{16}$$

Whereas the total external work done on the system based on Neumann boundary conditions Eqs. (12 – 14) is

$$\begin{aligned} \mathcal{W} = & \int_{\mathcal{V}} b_k u_k d\mathcal{V} + \int_{\mathcal{V}} q^e \phi d\mathcal{V} + \int_A t_i u_i dA + \int_A \bar{\omega} \phi dA \\ & + \int_A \bar{\tau}_i \nabla_{\mathbf{n}} u_i dA - \sum_\alpha \oint_{c^\alpha} [\![-m_j \tau_{ijk} n_k]\!] u_i dc. \end{aligned} \tag{17}$$

Then the total potential energy of the system Π is given as

$$\Pi = \int_{\mathcal{V}} \tilde{h} d\mathcal{V} - \mathcal{W}. \tag{18}$$

From Eqs. (8a and 7b), the existence of a fourth derivative of displacements in Eq.(18) can be postulated. This demands C^1-continuous elements which ensure continuity of mechanical strains. This cannot be modeled straightforwardly using traditional FEM. Mixed FEM can be used allowing usage of C^0-continuous elements for problems involving gradients. For this, mechanical strains are treated as independent variables, in contrast to computing them solely as displacement gradients. Such independently assumed strains are regarded as relaxed strains ψ_{ij} as they are observed to be smoothly varying across C^0-continuous elements in contrast to mechanical displacement gradients computed from mechanical displacements. Relaxed strains ψ_{ij} are utilized further for computing strain gradients $\tilde{\eta}_{ijk}$. Nevertheless, kinematic constraints are to be enforced between relaxed strains and mechanical displacement gradient for which Lagrange multipliers $\mathcal{L}_{ij}$ are used in a weighted residual manner. For such C^0-continuous elements, the kinematic constraints could only be enforced weakly. Therefore, the constraints for tangential component $\left[\psi_{ij}^t - u_{j,i}^t \right]$ are relaxed [1]. Also, for smooth surfaces without any discontinuities, the line integrals over curve c^α should be zero [38]. Total potential energy given in Eq. (18) enhanced with kinematic constraints $\mathcal{L}_{ij} \left[\psi_{ij} - u_{j,i} \right]$ takes the form:

$$\Pi^* = \int_{\mathcal{V}} \left[\frac{1}{2} \sigma_{ij} \varepsilon_{ij} + \frac{1}{2} \tau_{ijm} \tilde{\eta}_{ijm} + \frac{1}{2} \mathcal{D}_i^e E_i \right] d\mathcal{V}$$

$$- \int_{\mathcal{V}} b_k u_k d\mathcal{V} - \int_{\mathcal{V}} q^e \phi d\mathcal{V}$$

$$- \int_A t_i u_i dA - \int_A \bar{\omega} \phi dA - \int_A \bar{\tau}_i \nabla_{\mathbf{n}} u_i dA \qquad (19)$$

$$+ \int_{\mathcal{V}} \mathcal{L}_{ij} \left[\psi_{ij} - u_{j,i} \right] d\mathcal{V}.$$

In order to derive the equivalent weak form for the functional described in Eq. (19), the variational principle $\delta \Pi^* = 0$ is used along with the application of Reynold's transport theorem [37–39] leading to

$$\int_{\mathcal{V}} \left[\sigma_{ij} \delta \varepsilon_{ij} + \tau_{ijm} \delta \tilde{\eta}_{ijm} + \mathcal{D}_i^e \delta E_i \right] d\mathcal{V} - \int_{\mathcal{V}} b_k \delta u_k d\mathcal{V}$$

$$- \int_{\mathcal{V}} q^e \delta \phi d\mathcal{V} - \int_A t_i \delta u_i dA - \int_A \bar{\omega} \delta \phi dA$$

$$- \int_A \bar{\tau}_i \delta \nabla_{\mathbf{n}} u_i dA + \int_{\mathcal{V}} \delta \mathcal{L}_{ij} \left[\psi_{ij} - u_{j,i} \right] d\mathcal{V} \qquad (20)$$

$$+ \int_{\mathcal{V}} \mathcal{L}_{ij} \left[\delta \psi_{ij} - \delta u_{j,i} \right] d\mathcal{V} = 0.$$

Eq. (20) is the weak form that is the basis for describing mixed FEM and further computations.

4 Newly proposed finite elements: description and implementation

The finite element formulation for piezoelectric solids exhibiting flexoelectricity is developed based on Eq. (20). The weak form is discretized for variations of each independent variable, resulting in a set of linear equations that must be solved numerically. Since only the first derivatives of u_i, ψ_{ij}, ϕ exist in the weak form, C^1-continuity is nevertheless ensured by kinematic constraints. Various elements in the context of mixed FEM have been proposed for modeling flexoelectricity in dielectric solids [1, 28, 32–34]. However, the piezoelectric contribution was neglected.

All the finite elements analyzed in present work include flexoelectricity and piezoelectricity necessary for fully coupled electromechanical analyses. The elements developed in this work consist of mechanical displacements $[u_1, u_2]$, relaxed strains $[\psi_{11}, \psi_{21}, \psi_{12}, \psi_{22}]$, electric potential $[\phi]$, Lagrange multipliers $[\mathcal{L}_{11}, \mathcal{L}_{21}, \mathcal{L}_{12}, \mathcal{L}_{22}]$ as degrees of freedom (DOFs).
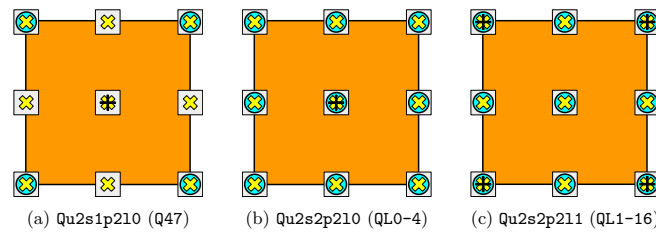
Three different forms of 9 noded quadrilateral elements have been used in this work as illustrated in Fig. 1 and described below:

1. Existing element referred as `Qu2s1p2l0` (Q47 according to [1]) comprises of 7 DOFs that include u_1, u_2, ψ_{11}, ψ_{21}, ψ_{12}, ψ_{22}, ϕ at corner nodes, 3 DOFs that include u_1, u_2, ϕ at midside nodes and 7 DOFs that include u_1, u_2, ϕ, $\mathcal{L}_{11}$, $\mathcal{L}_{21}$, $\mathcal{L}_{12}$, $\mathcal{L}_{22}$ at centre node. In this element, mechanical displacements and electric potential are interpolated using biquadratic shape functions, whereas relaxed strains are interpolated linearly. Lagrange multipliers are assumed to be constant across the element.

2. New element referred as `Qu2s2p2l0` (QL0-4) comprises of 7 DOFs that include u_1, u_2, ψ_{11}, ψ_{21}, ψ_{12}, ψ_{22}, ϕ at corner nodes, 7 DOFs that include u_1, u_2, ψ_{11}, ψ_{21}, ψ_{12}, ψ_{22}, ϕ at midside nodes and 11 DOFs that include u_1, u_2, ψ_{11}, ψ_{21}, ψ_{12}, ψ_{22}, ϕ, $\mathcal{L}_{11}$, $\mathcal{L}_{21}$, $\mathcal{L}_{12}$, $\mathcal{L}_{22}$ at centre node. In this element, mechanical displacements, relaxed strains, and electric potential are interpolated using biquadratic shape functions, whereas Lagrange multipliers are assumed to be constant across the element. The nomenclature QL0-4 denotes (Q)uadratic element with (L)agrange multiplier assumed to be constant (0) having (4) components per element.

3. New element referred as `Qu2s2p2l1` (QL1-16) comprises of 11 DOFs that include u_1, u_2, ψ_{11}, ψ_{21}, ψ_{12}, ψ_{22}, ϕ, $\mathcal{L}_{11}$, $\mathcal{L}_{21}$, $\mathcal{L}_{12}$, $\mathcal{L}_{22}$ at corner nodes, 7 DOFs that include u_1, u_2, ψ_{11}, ψ_{21}, ψ_{12}, ψ_{22}, ϕ at midside nodes and 7 DOFs that include u_1, u_2, ψ_{11}, ψ_{21}, ψ_{12}, ψ_{22}, ϕ at centre node. In this element, mechanical displacements, relaxed strains, and electric potential are interpolated using biquadratic shape functions, whereas Lagrange multipliers are interpolated linearly. The nomenclature QL1-16 denotes (Q)uadratic element with (L)agrange multiplier interpolated linearly (1) having (16) components per element.

The weak form given in Eq. (20) is discretized into elements for applying a finite element algorithm. In this section, "$\widehat{\bullet}$" corresponds to nodal quantities. Let "$\mathcal{V}^e$" represent an element. Collating all terms based on their respective independent variations brings

$$\int_{\mathcal{V}^e} \left[\delta \widehat{\varepsilon}^{\mathrm{T}} \{\sigma\} - \nabla \delta \widehat{u} \{\mathcal{L}\} \right] d\mathcal{V}^e$$

$$+ \int_{\mathcal{V}^e} \left[\delta \widehat{\psi}^{\mathrm{T}} \{\mathcal{L}\} + \delta \widehat{\tilde{\eta}}^{\mathrm{T}} \{\tau\} \right] d\mathcal{V}^e - \int_{\mathcal{V}^e} \delta \widehat{\phi}^{\mathrm{T}} \{q^e\} d\mathcal{V}^e$$

$$- \int_{\mathcal{V}^e} \left[\delta \widehat{E}^{\mathrm{T}} \{\mathcal{D}^e\} \right] d\mathcal{V}^e + \int_{\mathcal{V}^e} \delta \widehat{\mathcal{L}} \left[\{\psi\} - \{\nabla u\} \right] d\mathcal{V}^e$$

Fig. 1 Various forms of 9 noded quadrilateral Mixed FE: **a** Element with 47 DOFs `Qu2s1p2l0` (`Q47` according to [1]). **b** Element with 67 DOFs `Qu2s2p2l0` (`QL0-4`). **c** Element with 79 DOFs `Qu2s2p2l1` (`QL1-16`). (□) marks u_1 and u_2 DOFs whereas (◯) marks $\psi_{11}, \psi_{21}, \psi_{12}, \psi_{22}$ DOFs. (✗) marks ϕ DOF whereas (✚) marks $\mathcal{L}_{11}, \mathcal{L}_{21}, \mathcal{L}_{12}, \mathcal{L}_{22}$ DOFs

$$- \int_{\mathcal{V}^e} \delta \widehat{u}^{\mathrm{T}} \{b\} \, d\mathcal{V}^e - \int_{A^e} \delta \widehat{u}^{\mathrm{T}} \{\bar{t}\} \, dA^e$$

$$- \int_{A^e} \delta \widehat{\phi}^{\mathrm{T}} \{\bar{\omega}\} \, dA^e - \int_{A^e} \delta \nabla_{\mathbf{n}} \left(\widehat{u} \right)^{\mathrm{T}} \{\bar{\tau}\} \, dA^e = 0. \quad (21)$$

Eq. (21) is further simplified by neglecting tractions related to relaxed strains, and rewritten in terms of variations of independent variables using the corresponding connectivity and shape-function matrices:

$$\delta \widehat{u} \int_{\mathcal{V}^e} \left[\{B_u\}^{\mathrm{T}} \{\sigma\} - \{M_u\} \{\mathcal{L}\} \right] d\mathcal{V}^e$$

$$+ \delta \widehat{\psi} \int_{\mathcal{V}^e} \left[\{N_\psi\}^{\mathrm{T}} \{\mathcal{L}\} + \{B_\psi\}^{\mathrm{T}} \{\tau\} \right] d\mathcal{V}^e$$

$$- \delta \widehat{\phi} \int_{\mathcal{V}^e} \left[\{B_\phi\}^{\mathrm{T}} \{\mathcal{D}^e\} \right] d\mathcal{V}^e$$

$$+ \delta \widehat{\mathcal{L}} \int_{\mathcal{V}^e} \{N_{\mathcal{L}}\}^{\mathrm{T}} [\{\psi\} - \{\nabla u\}] \, d\mathcal{V}^e$$

$$- \delta \widehat{u} \int_{\mathcal{V}^e} \{N_u\}^{\mathrm{T}} \{b\} \, d\mathcal{V}^e$$

$$\underbrace{- \delta \widehat{\phi} \int_{\mathcal{V}^e} \{N_\phi\}^{\mathrm{T}} \{q^e\} \, d\mathcal{V}^e - \delta \widehat{u} \int_{A^e} \{N_u\}^{\mathrm{T}} \{\bar{t}\} \, dA^e}_{\mathrm{X}}$$

$$\underbrace{- \delta \widehat{\phi} \int_{A^e} \{N_\phi\}^{\mathrm{T}} \{\bar{\omega}\} \, dA^e}_{\mathrm{Y}} = 0. \quad (22)$$

Since the variations $\delta u, \delta \psi, \delta \phi, \delta \mathcal{L}$ are arbitrary, the following system of equations is obtained assuming no body force or free volume charges acting in the body:

$$\mathrm{G} \left(\widehat{u}, \widehat{\mathcal{L}}, \widehat{\phi} \right) = \underbrace{\int_{\mathcal{V}^e} \left[\{B_u\}^{\mathrm{T}} \{\sigma\} - \{M_u\} \{\mathcal{L}\} \right] d\mathcal{V}^e}_{\mathrm{F} \left(\widehat{u}, \widehat{\mathcal{L}}, \widehat{\phi} \right)}$$

$$\underbrace{- \int_{A^e} \{N_u\}^{\mathrm{T}} \{\bar{t}\} \, dA^e}_{\mathrm{X}} \stackrel{!}{=} 0, \quad (23a)$$

$$\mathrm{H} \left(\widehat{\psi}, \widehat{\mathcal{L}}, \widehat{\phi} \right) = \underbrace{\int_{\mathcal{V}^e} \left[\{N_\psi\}^{\mathrm{T}} \{\mathcal{L}\} + \{B_\psi\}^{\mathrm{T}} \{\tau\} \right] d\mathcal{V}^e}_{\mathrm{R} \left(\widehat{\psi}, \widehat{\mathcal{L}}, \widehat{\phi} \right)} \stackrel{!}{=} 0, \quad (23b)$$

$$\mathrm{I} \left(\widehat{u}, \widehat{\psi} \right) = \underbrace{\int_{\mathcal{V}^e} \{N_{\mathcal{L}}\}^{\mathrm{T}} [\{\psi\} - \{\nabla u\}] \, d\mathcal{V}^e}_{\mathrm{S} \left(\widehat{u}, \widehat{\psi} \right)} \stackrel{!}{=} 0, \quad (23c)$$

$$\mathrm{J} \left(\widehat{u}, \widehat{\psi}, \widehat{\phi} \right) = \underbrace{\int_{\mathcal{V}^e} \left[\{B_\phi\}^{\mathrm{T}} \{\mathcal{D}^e\} \right] d\mathcal{V}^e}_{\mathrm{V} \left(\widehat{u}, \widehat{\psi}, \widehat{\phi} \right)}$$

$$\underbrace{- \int_{A^e} \{N_\phi\}^{\mathrm{T}} \{\bar{\omega}\} \, dA^e}_{\mathrm{Y}} \stackrel{!}{=} 0. \quad (23d)$$

Linearization of the system of Eq. (23) for the Newton–Raphson scheme results in:

$$\{K_{uu}\} \widehat{u} + \{K_{u\mathcal{L}}\} \widehat{\mathcal{L}} + \{K_{u\phi}\} \widehat{\phi} = \{-\mathrm{F}\} + \{\mathrm{X}\},$$

$$\{K_{\psi\psi}\} \widehat{\psi} + \{K_{\psi\mathcal{L}}\} \widehat{\mathcal{L}} + \{K_{\psi\phi}\} \widehat{\phi} = \{-\mathrm{R}\},$$

$$\{K_{u\mathcal{L}}\}^{\mathrm{T}} \widehat{u} + \{K_{\psi\mathcal{L}}\}^{\mathrm{T}} \widehat{\mathcal{L}} = \{-\mathrm{S}\},$$

$$\{K_{u\phi}\}^{\mathrm{T}} \widehat{u} + \{K_{\psi\phi}\}^{\mathrm{T}} \widehat{\psi} + \{K_{\phi\phi}\} \widehat{\phi} = \{-\mathrm{V}\} + \{\mathrm{Y}\}, \quad (24)$$

where

- $\{K_{uu}\} = \int_{\mathcal{V}^e} \{B_u\}^{\mathrm{T}} \{\mathcal{C}\} \{B_u\} \, d\mathcal{V}^e$ corresponds to purely elastic stiffness coefficients,

- $\{K_{u\mathcal{L}}\} = -\int_{\mathcal{V}^e} \{M_u\}^T \{N_{\mathcal{L}}\}\, d\mathcal{V}^e$ corresponds to coefficients that relate mechanical displacement with Lagrange multipliers,

- $\{K_{u\phi}\} = \int_{\mathcal{V}^e} \{B_u\}^T \{d\} \{B_\phi\}\, d\mathcal{V}^e$ corresponds to piezoelectric coefficients,

- $\{K_{\psi\psi}\} = \int_{\mathcal{V}^e} \{B_\psi\}^T \{\mathcal{A}\} \{B_\psi\}\, d\mathcal{V}^e$ corresponds to SGE coefficients,

- $\{K_{\psi\mathcal{L}}\} = \int_{\mathcal{V}^e} \{N_\psi\}^T \{N_{\mathcal{L}}\}\, d\mathcal{V}^e$ corresponds to coefficients that relate relaxed strains to Lagrange multipliers,

- $\{K_{\psi\phi}\} = \int_{\mathcal{V}^e} \{B_\psi\}^T \{f\} \{B_\phi\}\, d\mathcal{V}^e$ corresponds to flexoelectric coupling coefficients,

- $\{K_{\phi\phi}\} = -\int_{\mathcal{V}^e} \{B_\phi\}^T \{\kappa\} \{B_\phi\}\, d\mathcal{V}^e$ corresponds to dielectric coefficients,

- $\{B_u\}, \{B_\psi\}, \{B_\phi\}$ are the differential matrices used to compute mechanical strains, relaxed strain gradients, and electric field from $\widehat{u}, \widehat{\psi}, \widehat{\phi}$, respectively.

From Eq. (24), the element stiffness matrix AMATRX, degrees of freedom vector DOFs and RHS vector are given as

$$
\text{AMATRX} = \begin{bmatrix} K_{uu} & 0 & K_{u\mathcal{L}} & K_{u\phi} \\ 0 & K_{\psi\psi} & K_{\psi\mathcal{L}} & K_{\psi\phi} \\ K_{u\mathcal{L}}^T & K_{\psi\mathcal{L}}^T & 0 & 0 \\ K_{u\phi}^T & K_{\psi\phi}^T & 0 & K_{\phi\phi} \end{bmatrix},
$$

$$
\text{DOFs} = \begin{bmatrix} \widehat{u} \\ \widehat{\psi} \\ \widehat{\mathcal{L}} \\ \widehat{\phi} \end{bmatrix}, \quad \text{RHS} = \begin{bmatrix} -F \\ -R \\ -S \\ -V \end{bmatrix} + \begin{bmatrix} X \\ 0 \\ 0 \\ Y \end{bmatrix}. \tag{25}
$$

The algorithm of mixed FE for flexoelectricity in piezoelectric solids is given in Algorithm 1. In the current research, the Direct Sparse Solver is used as a general purpose solver with distinguished stability for efficiently solving the system of equations.

5 Numerical simulations

In this section, new mixed FEM implementation is verified against various benchmark problems, such as thick cylinder, truncated pyramid and cantilever beam problems. A thick cylinder problem is used for the verification of flexoelectricity in dielectric solids (sheer higher-order electromechanical coupling). A truncated pyramid is used to verify the implementation taking into account all components of strain gradients. Afterwards, a cantilever beam problem is used for the verification of flexoelectricity in piezoelectric solids (combined linear and higher-order electromechani-

---

Algorithm 1 Mixed FE subroutine

1: Initialize DOFs $u_i, \psi_{ij}, \mathcal{L}_{ij}, \phi$ ▷ from previous time step
2: Calculate $\mathcal{C}, \mathcal{A}, \kappa, d, f$ ▷ material tensors
3: **for** i=1, Gauss points **do**
4:    Calculate $N_u, N_\psi, N_{\mathcal{L}}, N_\phi$ ▷ quadratic shape functions
5:    Calculate jacobian matrices, its determinant
      and inverse
6:    Calculate B_u, B_ψ, B_ϕ ▷ differential matrices
7:    Calculate M_u ▷ gradient matrix of displacement
8:    Calculate $\varepsilon_{ij}, u_{i,j}, \tilde{\eta}, E_i, \mathcal{L}_{ij}$ ▷ strain-like variables and Lagrange multiplier
9:    Calculate $\sigma_{ij}, \tau_{ijk}, \mathcal{D}_i^e$ based on Eq. (7)   ▷ stress-like variables
10:    Evaluate F, X, R, S, V, Y based on Eq. (23)
11:    Update RHS vector based on Eq. (25)
12:    Calculate $K_{uu}, K_{u\mathcal{L}}, K_{u\phi}, K_{\psi\psi}, K_{\psi\mathcal{L}}, K_{\psi\phi}, K_{\phi\phi}$
      based on Eq. (24) ▷ component matrices of element stiffness matrix
13:    Update AMATRX matrix based on Eq. (25)
14: **end for**
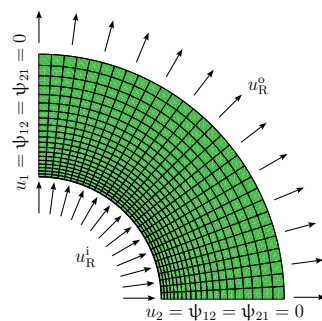15: **return** AMATRX, RHS

Fig. 2 Geometric illustration of the thick cylinder problem with 600 elements

cal coupling). Finally, a comparison of the existent element Q47 with newly proposed elements is performed to illustrate the robustness of the proposed finite elements.

5.1 Thick cylinder: dielectric solids with flexoelectric effect

In this subsection, the user element is verified for the case of flexoelectricity in dielectric solids in the absence of piezoelectricity. Also, as no piezoelectricity is considered, it is an isotropic case. For this, a classical BVP of a thick cylinder with prescribed inner and outer radial displacements is considered [1]. It is possible to obtain an analytical solution for this axis-symmetric problem. Analytical solution for the primary variable u_R for SGE is given in [40]. It was further extended for flexoelectric solids with electric polarization as local variable [41]. The analytical solution for flexoelectric solids with electric field as local variable is given in [1].

The geometric illustration of the quarter symmetry meshed model used for the numerical simulation and applied boundary conditions is shown in Fig. 2. It is an axis-symmetric problem with a 2D plane strain assumption. Details related

Table 1 Thick cylinder: geometry details and applied loading

Property	Inner boundary	Outer boundary
Radius	$r^i = 10 \; \mu m$	$r^o = 20 \; \mu m$
Displacement	$u^i_R = 0.045 \; \mu m$	$u^o_R = 0.05 \; \mu m$
Electric potential	$\phi^i = 0.0$ V	$\phi^o = 1.0$ V

Table 2 Material properties of the thick cylinder [1]

Y [GPa]	ν	l [μm]	f_1, f_2 [C/m]	κ_{11}, κ_{22} [F/m]
139	0.3	2	1×10^{-6}	1×10^{-9}

to the simulation model are summarised in Table 1. Superscripts i and o correspond to inner and outer geometrical quantities, respectively. The numerical simulations are performed using all three elements: Q47, QL0-4, QL1-16. Table 2 summarizes the material properties used. Here, Y is Youngs modulus, ν is Poissons ratio, l is the material length scale, f_1, f_2 are the flexoelectric coefficients, κ_{11}, κ_{22} are the dielectric coefficients. The results for the mechanical displacements and electric potential from the numerical simulations are compared with known analytical solution, cf. Fig. 3. The comparison shows high correlation for all types of finite elements. Furthermore, the electric field distribution is presented in Fig. 4. Flexoelectricity has a powerful influence due to its dependence on strain gradients which are inversely proportional to the length scale. This increases the material's stiffness, yielding lower displacement through the thickness of the beam. A steep rise in the electric field near the inner surface of the cylinder is appealing to observe. It is essential to state that since this example is defined at micrometer length scale, stabilization diagonal parameter α in the order of 10^{-22} is required here for the known element Q47, cf. Sect. 5.5. The distribution of the radial and circumferential components of relaxed and mechanical strains is shown in Figs. 5 and 6. From Fig. 5, it can be observed that there is prominent waviness in the plot of the radial component of mechanical strain ε_{11} for Q47 due to weak enforcement of kinematic constraints which is also acknowledged in [1]. This waviness in the proximity of the outer surface does not exist in the case of the proposed elements QL0-4 and QL1-16. There is a non-smooth distribution in the proximity of the inner surface for the elements Q47 and QL0-4 which does not occur in case of the element QL1-16. QL0-4 and QL1-16. For comparing the computational cost using a test thick cylinder job with 600 elements on a standard desktop[1], it is observed that Q47 takes 3.32 s / 60 MB, whereas QL0-4 – 3.59 s / 90 MB, and QL1-16 – 4.27 s / 112

MB RAM. Hence, it can be stated that QL1-16 yields best results at the expense of acceptably higher computational cost.

## 5.2 Truncated pyramid: pure flexoelectric effect without SGE

A truncated pyramid sets an excellent example for inducing strain gradients under compression. The same was used for performing experiments to quantify longitudinal flexoelectric coefficient in [17]. This example considers a 2D truncated pyramid under plane strain assumption. The top surface has a length equal to the pyramid's height, whereas the bottom has a length of three times that of the height. The bottom surface is fixed along both directions, and an applied compressive force F = −4.5 N is distributed along the length of the top surface [3]. The top surface is electrically grounded. A small value of $10^{-3} \times l$ is used for numerical stability [3, 27]. The geometry is meshed with a total of 2500 elements. The tapered edges are meshed with a bias ratio of 3, whereas a uniform mesh is utilized on the top and bottom edges, ensuring a consistent element count of 50 on each of these edges. For the sake of verification with results from available literature the exactly same simulation setup is used. This assumption of negligible material length scale excludes the complexities involved due to consideration of SGE. Such a scenario is referred to as pure flexoelectric effect [1]. With this, the energy contribution due to SGE is ignored as a consequence of resulting $\mathcal{A}_{jklmni} \approx 0$ in Eq. (7b). Nevertheless, relaxed strains are still computed and kinematically constrained with mechanical strains to evaluate strain gradients and, consequently, the flexoelectric contribution.

Table 3 summarizes the material properties used. Figure 7 shows the schematic illustration of the geometric details and boundary conditions.

As a result of the difference in length between the upper and lower side, inhomogeneous strains occur in the truncated pyramid, which lead to strain gradients in the longitudinal direction. Also, fixing the bottom surface yields inhomogeneous traction distribution supporting the development of strain gradients. Due to this, $\tilde{\eta}_{333}$ is significant here. In the case of flexoelectricity, there are three independent flexoelectric coefficients due to the cubic symmetry of the flexoelectric tensor. These coefficients include f_{1111}, f_{1331}, f_{1313} that are denoted as f_{11}, f_{12}, f_{44} in Voigt notation. Under isotropic assumption, $f_{11} = f_1 + 2f_2$, $f_{12} = f_1$, $f_{44} = 2f_2$ [1, 3]. Flexoelectric constants f_1 and f_2 are analogous to Lame's constants for linear elasticity in isotropic materials. However, shear component $f_2 = f_{1313} = f_{44}$ is neglected here for the verification purpose with results of [3]. In order to assess the implications of flexoelectricity, an effective electric field across truncated pyramid is evaluated as $E_{\text{eff}} = V/h$, where V is the electric potential difference between the top and

---

[1] Intel(R) Xeon(R) E5-2630 v2 @ 2.60 GHz with 32 Gigabytes of RAM.

Fig. 3 Comparison of the mechanical displacement (left) and electric potential (right) in the radial direction from the numerical simulations with analytical solution
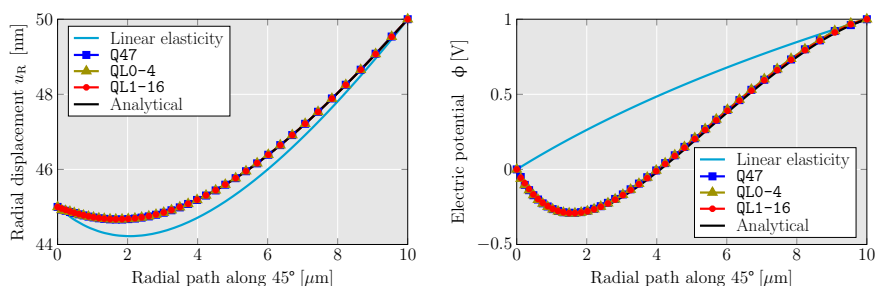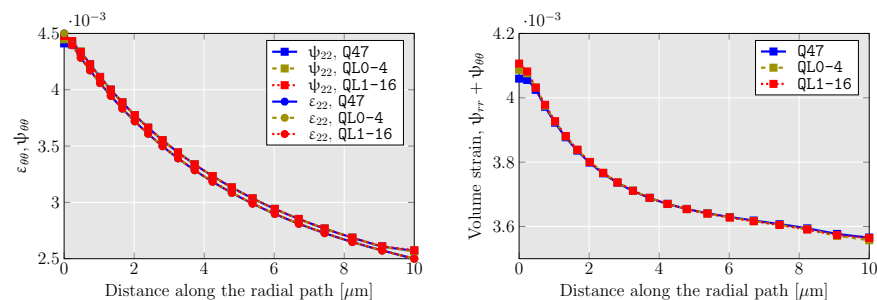

Fig. 4 Electric field in the radial direction (left) and the corresponding electric potential contour (right)
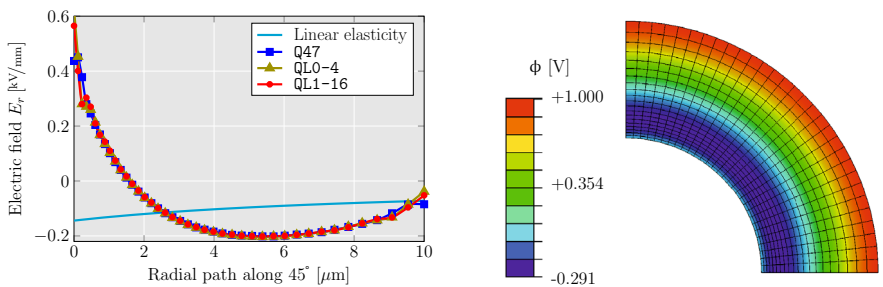
Fig. 5 Comparison of mechanical ε_{11} and relaxed ψ_{11} strain component (left) and relaxed ψ_{11} strain contour (right)
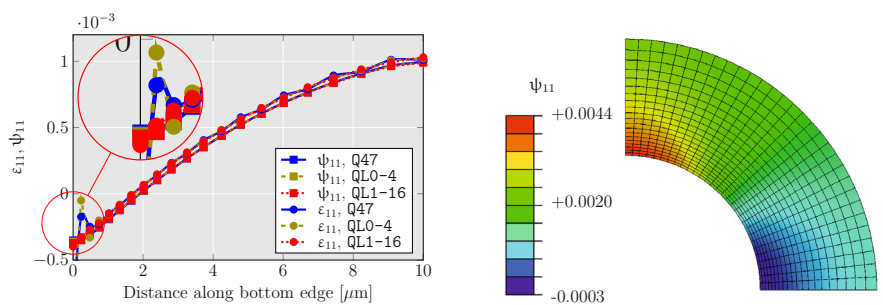
Fig. 6 Circumferential (left) and volume (right) strain in the presence of flexoelectricity

bottom surface generated due to the flexoelectricity. Also, ϕ is assumed to be constant along the bottom surface as a result of a sensing electrode attached to it. The effective electric field E_{eff} is evaluated for various sizes of the truncated pyramid and compared with the simulation presented in [3, 27]. The results of the verification are shown in Fig. 8. The size-dependent phenomenon of flexoelectricity is comprehensively illustrated in this graph. Moreover, it can be seen that the results of the numerical modeling are in great agreement with those given in the literature. The contour plot for the electric potential distribution provide an additional illustration of the pure flexoelectric effect impact (the height of

Table 3 Material properties of the truncated pyramid [27]

Y [GPa]	ν	f_1 [C/m]	f_2 [C/m]	κ_{11}, κ_{33} [F/m]
100	0.37	1×10^{-6}	0	11×10^{-9}

the pyramid is taken to be 7.5 μm) and matches the known results.

5.3 Cantilever beam: piezoelectric solids with flexoelectric effect

As one of the important points of this work is to study the mutual interaction between piezoelectricity and flexo-
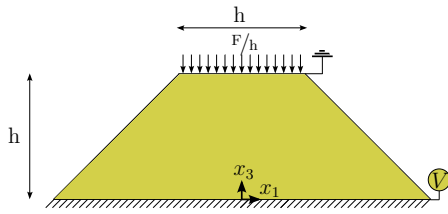
Fig. 7 Geometric illustration of the truncated pyramid problem

electricity, verifying the material behavior when both are activated simultaneously is important.

In [42], the electromechanical coupling factor k_{eff} for 1D flexoelectric cantilever beam neglecting any 2D effects is derived analytically as
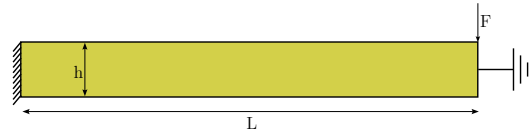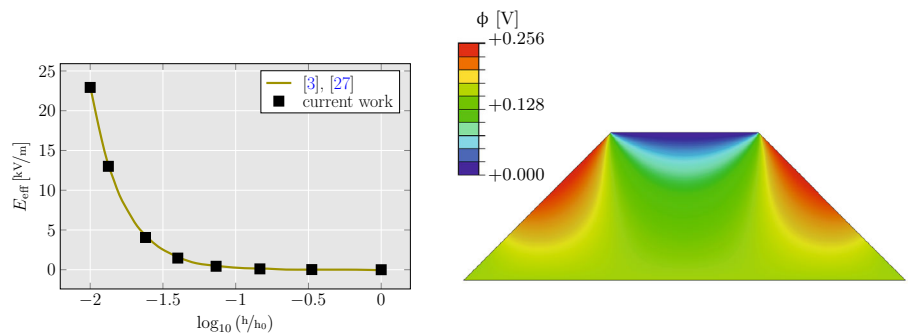
$$k_{\text{eff}} = \frac{\chi}{1+\chi} \sqrt{\frac{1}{\kappa Y} \left[d_{31}^2 + 12 \left[\frac{f_1}{h} \right]^2 \right]}. \tag{26}$$

χ is the relative electric susceptibility. In case of the numerical simulations, k_{eff} is computed as

$$k_{\text{eff}} = \frac{\frac{1}{2} \int\limits_{\mathcal{V}^e} E_i \kappa_{ij} E_j d\mathcal{V}^e}{\frac{1}{2} \int\limits_{\mathcal{V}^e} \varepsilon_{kl} \mathcal{C}_{klmn} \varepsilon_{mn} d\mathcal{V}^e}. \tag{27}$$

Figure 9 illustrates the geometry of the cantilever beam and the applied loading used in the current work. The material properties are summarized in Table 4. The ratio $L/h = 20$ is used for this analysis. A small value of l is used for numerical stability similar to Sect. 5.2. As the relation for k_{eff} (Eq. (26)) is based on 1D, the 2D effects of the cantilever beam problem are to be neglected and only $\tilde{\eta}_{311}$ is relevant here. Concentrated force F is applied at the free end of the cantilever beam. The geometry is meshed with a total of 2000 elements. The mesh consists of 10 layers of elements along the height of the cantilever beam, while each edge along its length comprises 200 elements.

Fig. 9 Geometric illustration of cantilever beam problem

Table 4 Material properties of the cantilever beam [3]

Y [GPa]	ν	f_1 [C/m]	f_2	κ_{11}	κ_{22} [F/m]	χ	d_{31} [C/m²]
100	0.0	1×10^{-6}	0.0	0.0	12.48×10^{-9}	1408	-4.4

The normalized effective piezoelectric constant is computed as [42]:

$$\widetilde{d} = k_{\text{eff}}/k_{\text{eff}}^{\text{piezo}}, \tag{28}$$

where $k_{\text{eff}}^{\text{piezo}}$ is calculated by only activating piezoelectricity without flexoelectricity.

The results of the simulations and various comparisons are shown in Figs. 10 and 11. It can be seen that the results are in great agreement with the analytical solution and the numerical calculations. The aim is to illustrate the size-dependent behavior of flexoelectricity. The existence of an additional linear electromechanical coupling has a significant influence only for larger geometrical sizes. Figure 11 shows the normalized effective piezoelectric constant vs. normalized length/height of the beam. It can be concluded that flexoelectricity is very prominent at smaller scales of study and has a negligible influence at larger scales. However, there is an overestimation of the piezoelectric coefficient due to the absence of 2D effects, which was as well acknowledged in [3]. With this, the implementation of a fully coupled electromechanical formulation is additionally verified.

5.4 Truncated pyramid: piezoelectric solids with flexoelectric effect

In the current subsection, the analysis of piezoelectric truncated pyramid with activation of flexoelectricity is performed for the first time. The geometry and boundary conditions are

Fig. 8 Verification of the normalized effective piezoelectric constant (left) in which, $h_0 = 750 \ \mu$m is used for normalizing heights of truncated pyramids on the abscissa. Contour plot of the generated electric potential distribution (right)

Fig. 10 Distribution of electric potential ϕ (top) and electric field E_2 (bottom) for piezoelectricity + flexoelectricity case with h = 0.273 μm
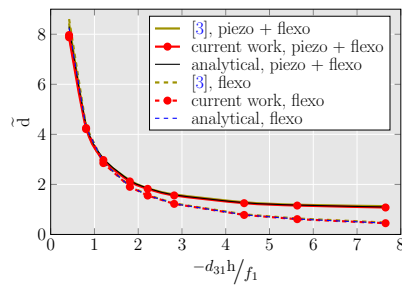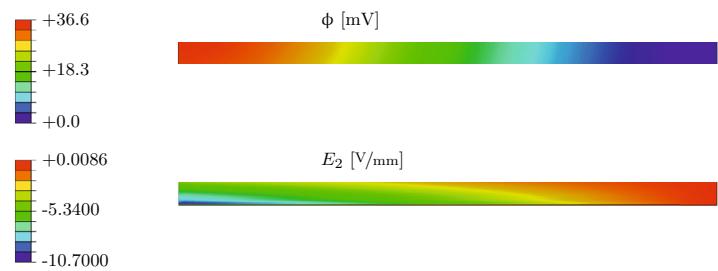
Fig. 11 Comparison of simulation of a cantilever beam problem with analytical solution [42] and numerical results [3]

illustrated in Fig. 7, cf. Sect. 5.2. A compressive force of −4.5 nN is applied, whereas h = 1500 nm and l = 2 nm. A transversely isotropic Aluminum Nitride (AlN) piezoelectric ceramic poled along positive x_3 direction is considered. The material properties are summarized in Table 5.

Truncated pyramid is a complex problem due to tapering edges acting as sites for sheer strain gradients. This greatly influences the electric potential generated due to flexoelectricity. In case of linear electromechanical coupling scenarios, the tapering edges act as stress and electric field concentrations zones. The aim of the current study is the analysis of the mutual interaction of flexoelectricity and piezoelectricity.

The results obtained are shown in Fig. 12. The linear and higher-order electromechanical influences are visible in the contour diagrams. For the electric potential plotted along x_3- coordinate and tapered edge of the truncated pyramid at $x_1 = 0$, the superpositional nature of piezoelectricity and flexoelectricity is observed. The diagram emphasizes the difference between the spatial distribution of the electric field due to linear and higher-order electromechanical coupling. It is stated that the influence of each of these phenomenon is dependent on the scale of study, e.g., for truncated pyramid with h = 7.5 μm, piezoelectric effect is stronger than flexoelectric effect and hence former overshadows the latter. Whereas, for truncated pyramid with h = 7.5 nm, the flexoelectric effect is essentially more pronounced than the piezoelectric effect. For this reason, a truncated pyramid with midrange size of h = 1.5μm, for which the orders of influence are of the same magnitude, is chosen to illustrate the interaction between these phenomena. With this study,

it is emphasized that flexoelectricity in piezoelectric solids is more of a geometric-size dependent phenomena rather than that of material properties. Simulations through different scales, ranging from dominant linear electromechanical coupling on the macro and mesoscale down to gradient-dominated simulations on the nanoscale, are now possible in a single numerical framework. The proposed elements make it possible to isolate the influence of piezoelectricity and flexoelectricity independently, which is crucial for modern miniaturized electronics.

5.5 Comparison of the existing element Q47 with newly proposed elements for flexoelectricity: analysis of stabilization parameter α

Current subsection illustrates the influence of stabilization parameter on the performance of Q47[1]. The diagonal zeros in element stiffness matrix given in Eq. (24) have to be replaced with small numerical zeros to assure numerical stability. Such numerical zero quantity is referred to as stabilization parameter. The challenge with Q47 is that the stabilization parameter is problem / length scale specific and simulations in the case of non-suitable stabilization parameter magnitude can produce inaccurate results. To illustrate such behavior, the thick cylinder problem from Sect. 5.1 is simulated with various stabilization magnitudes α, while all other parameters are kept unchanged. This comparison is conducted for the distribution of mechanical strain ε_{11} and relaxed strain ψ_{11} across the thickness of the cylinder and presented in Fig. 13. It is expected that the distribution of ε_{11} and ψ_{11} will overlap due to the application of kinematic constraints. However, due to the weak enforcement of such constraints within a finite element, small deviations are possible [1].

A brief summary of the results using various stabilization parameters for existing element Q47 is shown in Table 6. It can be observed that the constraints are not obeyed at all when $\alpha = 0.0$. In contrast, in case of QL0-4 and QL1-16, the constraints for $\alpha = 0.0$ are fulfilled (i.e. there is no need for a stabilisation parameter), as can be seen from Fig. 5. Using stabilisation parameter larger than 10^{-15} yields a severe discrepancy between the mechanical strains and the relaxed

Table 5 Material properties of Aluminum Nitride piezoelectric ceramic poled along x_3 direction [43] with flexoelectricity

$\mathcal{C}_{11}$	$\mathcal{C}_{12}$	$\mathcal{C}_{22}$	$\mathcal{C}_{13}$	$\mathcal{C}_{66}$ [GPa]	κ_{11}	κ_{33} [nF/m]	d_{15}	d_{31}	d_{33} [C/m²]	f_2	f_1 [C/m]
345	125	395	120	110	0.08	0.095	-0.48	-0.58	1.55	0.0	1×10^{-6}

Fig. 12 Contour plot of the generated electric potential for piezoelectric case (top left), flexoelectric case (top right), combination of piezoelectric and flexoelectric cases (bottom left) and comparison of generated electric potential across truncated pyramid for different cases (bottom right). Here "V" stands for the electric potential values extracted along the x_3-coordinate, while "TE" - along tapered edge, starting from bottom up
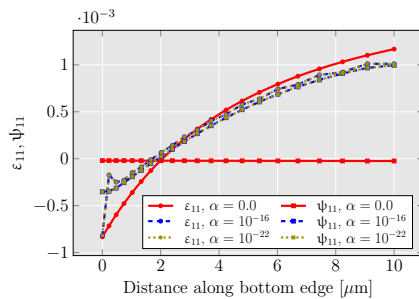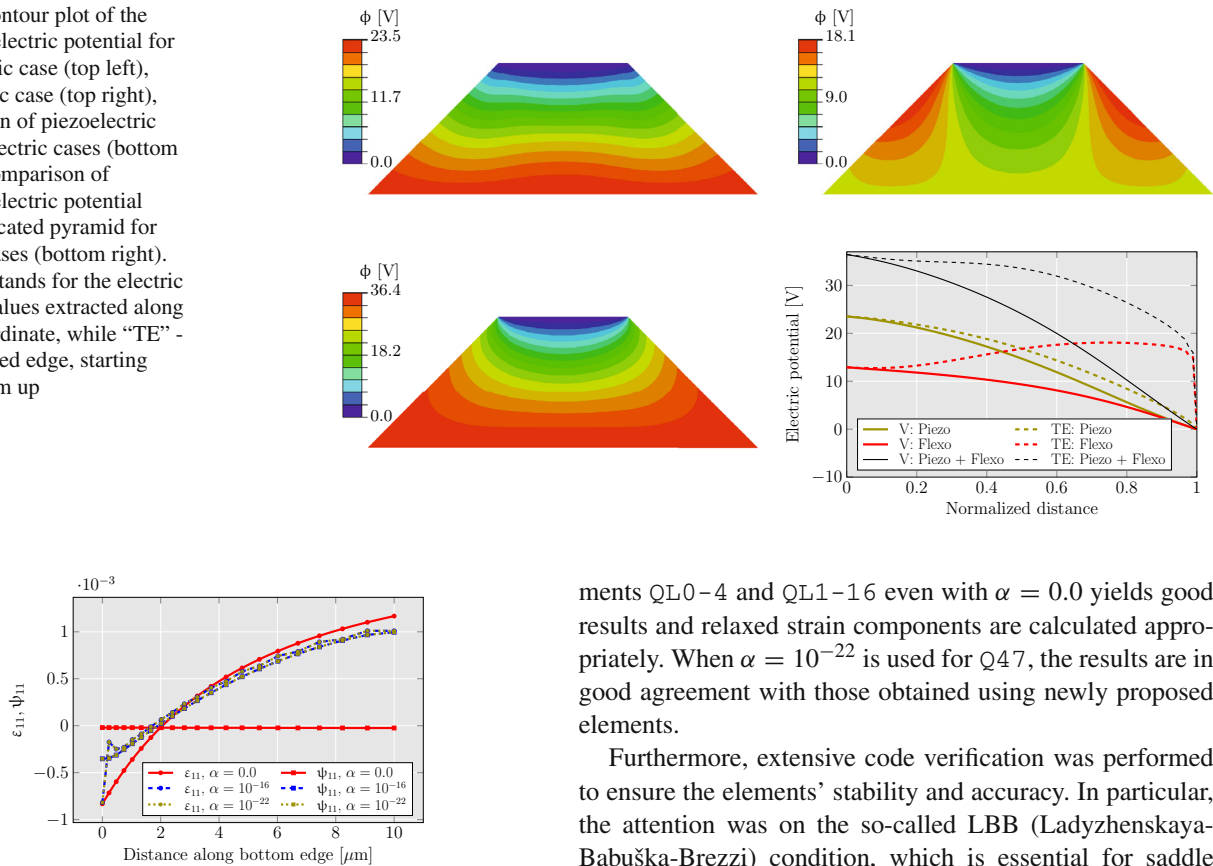
Fig. 13 Comparison of mechanical and relaxed strain components for various stabilization parameters

strains. It must also be recalled that α is strongly dependent on the length scale of the BVP.

Another example used to illustrate the influence of stabilization parameter is cantilever beam with an applied concentrated force F = 100 μN on its free end as shown in Fig. 9. The cantilever beam is assumed to have L/h = 25. The material properties used for this analysis are summarised in Table 7 and are assumed to be the same throughout the study.

The main purpose here is to compare the deflection profile of the cantilever beam for the existing element and for the newly proposed elements. The results obtained are shown in Fig. 14.

From Fig. 14, it can be observed that for Q47 with $\alpha = 0.0$, the results have very large deviation. This happens because the kinematic constraints are not obeyed and the relaxed strain components ψ_{ij} are not calculated correctly. On the other hand, the results of the newly proposed ele-

ments QL0-4 and QL1-16 even with $\alpha = 0.0$ yields good results and relaxed strain components are calculated appropriately. When $\alpha = 10^{-22}$ is used for Q47, the results are in good agreement with those obtained using newly proposed elements.

Furthermore, extensive code verification was performed to ensure the elements' stability and accuracy. In particular, the attention was on the so-called LBB (Ladyzhenskaya-Babuška-Brezzi) condition, which is essential for saddle point problems like the one at hand. Passing the patch test, as advocated in [44], serves as a key indicator of fulfilling the LBB condition. The patch test is a standard procedure in FE analysis that involves constructing a small patch of elements with known analytical solutions or expected behavior. By applying appropriate boundary conditions, the computed results are compared with the expected solutions. As part of the code verification process, patch tests were performed using bi-quadratic mechanical displacement and electric potential. The proposed elements successfully passed these rigorous tests, providing strong evidence of their numerical robustness without the need for additional stabilization parameters.

6 Conclusion

In the current research, two new numerically robust finite elements for fully coupled higher-order electromechanical simulations are proposed.

Table 6 Summary of results for various stabilization parameters

α	10^{-10} to 10^{-15}	10^{-16} to 10^{-22}	0.0
Results	Not realistic compared to results given in literature.	Realistic & matching results within the given range.	Large deviation in results as kine-matic constraints are not obeyed.

Table 7 Material properties of the cantilever beam [1, 28]

Y [GPa]	ν	l [nm]	$f_1 = f_2$ [C/m]	$\kappa_{11} = \kappa_{22}$ [F/m]
126	0.3	2	1×10^{-6}	13×10^{-9}
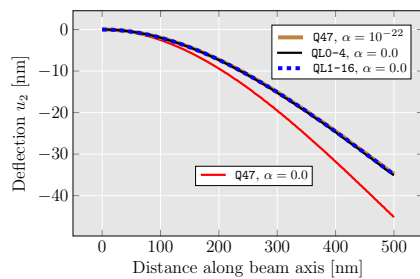
Fig. 14 Comparison of deflection of beam for existing and newly proposed finite elements

This involves not only the established flexoelectric formulations in dielectric solids, but on top of that an additional linear electromechanical coupling (piezoelectricity).

For dielectric insulator materials with non-cubic unit cell structures such as tetragonal or rhombohedral ones, there exists an intrinsic non-centrosymmetry leading to piezoelectricity in addition to a flexoelectricity due to mechanical or electrical gradients. Some tentative attempts have shown that it is possible to capture these two phenomena, but most of this research has not been explored in detail. The present manuscript makes a significant contribution to the field of flexoelectricity in several ways, including new stable mixed finite elements for direct incorporation of both linear and higher order coupling, with results that highlight the interactions between piezoelectricity and flexoelectricity at different length scales through in-depth analysis.

The variational formulations of flexoelectricity along with piezoelectricity involve fourth-order partial differential equations. Therefore, a mixed FEM is employed so that C^0-continuous elements can be used, which weakly ensure C^1-continuity. Two new finite elements `QL0-4` and `QL1-16` are introduced and their robustness is illustrated. In addition, the existing finite element `Q47` is implemented from scratch to replicate results from the literature and to gain further information on numerical stability. Our work has shown that the existing elements rely on a stabilisation parameter, while the newly proposed elements do not.

The reliability of new elements was demonstrated by their application to known benchmark problems such as a thick cylinder and a cantilever beam. The numerical results show a great agreement with the analytical solution for the thick cylinder problem and those from the literature.

In addition, an analysis for a piezoelectric truncated pyramid with flexoelectricity is performed for the first time. The study yielded a scale-dominated profile of the generated electric potential for the case where flexoelectricity is activated in piezoelectric material, and enabled simulations to be performed at the macroscale, where the flexoelectric contribution is negligible and only linear piezoelectric coupling takes place, and at the intermediate scale, where it depends on the mutual values of the piezoelectric, dielectric and flexoelectric tensor components, so that the influence becomes comparable, all the way down to nanostructural simulations, where the flexoelectric effect can have a purely dominant effect, depending on the geometry and loading.

It is shown that it is possible to separate piezoelectricity and flexoelectricity with the proposed finite elements. Such analyses are important because it is difficult to isolate different phenomena in experiments.

It can be concluded that the proposed numerical modeling enabled the insight into the size-dependent interactions of different phenomena using the newly developed numerically robust mixed finite elements. The current research highlights the importance of the existing non-centrosymmetry in the nanoscale single crystals or the genuine polarisation of industrially used polycrystalline ceramics possessing linear electromechanical coupling on the overall electromechanical response of MEMS with flexoelectricity.

Currently, work is underway to incorporate the non-linear ferroelectric material behaviour within flexoelectric formulations.

Declarations

Competing financial interests The authors declare that they have no known competing financial interests or personal relationships that could have appeared to influence the work reported in this paper.

References

1. Deng F, Deng Q, Yu W, Shen S (2017) Mixed Finite Elements for Flexoelectric Solids. J Appl Mech 84(8):081004. https://doi.org/10.1115/1.4036939
2. Mason WP (1981) Piezoelectricity, its history and applications. J Acoust Soc Am 70(6):1561–1566. https://doi.org/10.1121/1.387221
3. Abdollahi A, Peco C, Millán D (2014) Computational evaluation of the flexoelectric effect in dielectric solids. J Appl Phys. https://doi.org/10.1063/1.4893974
4. Mashkevich V, Tolpygo K (1957) Electrical, optical and elastic properties of diamond type crystals. Sov Phys JETP 5(3):435–439
5. Kogan SM (1964) Piezoelectric effect during inhomogeneous deformation and acoustic scattering of carriers in crystals. Soviet Physics-Solid State 5(10):2069–2070
6. Ma W, Cross LE (2001) Observation of the flexoelectric effect in relaxor Pb(Mg1/3Nb2/3)O3 ceramics. Appl Phys Lett 78(19):2920–2921. https://doi.org/10.1063/1.1356444
7. Ma W, Cross LE (2002) Flexoelectric polarization of barium strontium titanate in the paraelectric state. Appl Phys Lett 81(18):3440–3442. https://doi.org/10.1063/1.1518559
8. Ma W, Cross LE (2005) Flexoelectric effect in ceramic lead zirconate titanate. Appl Phys Lett 86(7):072905. https://doi.org/10.1063/1.1868078
9. Profant T, Sládek J, Sládek V, Kotoul M (2023) Assessment of amplitude factors of asymptotic expansion at crack tip in flexoelectric solid under mode I and II loadings. Int J Solids Struct 269:112194. https://doi.org/10.1016/j.ijsolstr.2023.112194
10. Kozinov S, Kuna M (2018) Simulation of fatigue damage in ferroelectric polycrystals under mechanical/electrical loading. J Mech Phys Solids 116:150–170. https://doi.org/10.1016/j.jmps.2018.03.013
11. Zubko P, Catalan G, Tagantsev AK (2013) Flexoelectric Effect in Solids. Annu Rev Mater Res 43(1):387–421. https://doi.org/10.1146/annurev-matsci-071312-121634
12. Kozinov S, Kuna M (2015) Simulation of damage in ferroelectric actuators by means of cohesive zone model. Sens Actuators A 233:176–183. https://doi.org/10.1016/j.sna.2015.06.030
13. Cosserat E (1909) Théorie des corps déformables. Librairie Scientifique A, Hermann et Fils
14. Toupin RA (1956) The elastic dielectric. J Ration Mech Anal 5(6):849–915. https://doi.org/10.1512/iumj.1956.5.55033
15. Mindlin RD (1964) Micro-structure in linear elasticity. Arch Ration Mech Anal 16(1):51–78. https://doi.org/10.1007/BF00248490
16. Zhuang X, Nguyen BH, Nanthakumar SS, Tran TQ, Alajlan N, Rabczuk T (2020) Computational Modeling of Flexoelectricity - A Review. Energies 13(6):1326. https://doi.org/10.3390/en13061326

17. Cross LE (2006) Flexoelectric effects: charge separation in insulating solids subjected to elastic strain gradients. J Mater Sci 41(1):53–63. https://doi.org/10.1007/978-0-387-38039-1_5
18. Zhu W, Fu JY, Li N, Cross L (2006) Piezoelectric composite based on the enhanced flexoelectric effects. Appl Phys Lett 89(19):192904. https://doi.org/10.1063/1.2382740
19. Ray M (2014) Exact solutions for flexoelectric response in nanostructures. J Appl Mech 10(1115/1):4027806. https://doi.org/10.1115/1.4027806
20. Hughes TJ, Cottrell JA, Bazilevs Y (2005) Isogeometric analysis: cad, finite elements, nurbs, exact geometry and mesh refinement. Comput Methods Appl Mech Eng 194(39):4135–4195. https://doi.org/10.1016/j.cma.2004.10.008
21. Agrawal V, Gautam SS (2019) IGA: a Simplified introduction and implementation details for finite element users. J Inst Eng (India) Ser C 100(3):561–585. https://doi.org/10.1007/s40032-018-0462-6
22. Ghasemi H, Park HS, Rabczuk T (2017) A level-set based IGA formulation for topology optimization of flexoelectric materials. Comput Methods Appl Mech Eng 313:239–258. https://doi.org/10.1016/j.cma.2016.09.029
23. Thai TQ, Rabczuk T, Zhuang X (2018) A large deformation isogeometric approach for flexoelectricity and soft materials. Comput Methods Appl Mech Eng 341:718–739. https://doi.org/10.1016/j.cma.2018.05.019
24. Thai TQ, Zhuang X, Park HS, Rabczuk T (2021) A staggered explicit-implicit isogeometric formulation for large deformation flexoelectricity. Eng Anal Boundary Elem 122:1–12. https://doi.org/10.1016/j.enganabound.2020.10.004
25. Nguyen-Thanh N, Nguyen-Xuan H, Bordas SPA, Rabczuk T (2011) Isogeometric analysis using polynomial splines over hierarchical T-meshes for two-dimensional elastic solids. Comput Methods Appl Mech Eng 200(21–22):1892–1908. https://doi.org/10.1016/j.cma.2011.01.018
26. Yvonnet J, Liu L (2017) A numerical framework for modeling flexoelectricity and maxwell stress in soft dielectrics at finite strains. Comput Methods Appl Mech Eng 313:450–482. https://doi.org/10.1016/j.cma.2016.09.007
27. Codony D, Marco O, Fernández-Méndez S, Arias I (2019) An immersed boundary hierarchical B-spline method for flexoelectricity. Comput Methods Appl Mech Eng 354:750–782. https://doi.org/10.1016/j.cma.2019.05.036
28. Tian X, Sladek J, Sladek V, Deng Q, Li Q (2021) A collocation mixed finite element method for the analysis of flexoelectric solids. Int J Solids Struct 217–218:27–39. https://doi.org/10.1016/j.ijsolstr.2021.01.031
29. Sladek J, Sladek V, Repka M, Pan E (2022) Size effect in piezoelectric semiconductor nanostructures. J Intell Mater Syst Struct 33(11):1351–1363. https://doi.org/10.1177/1045389X211053049
30. Tannhäuser K, Serrao PH, Kozinov S (2023) Second-order collocation-based mixed fem for flexoelectric solids. Special Issue "Recent Advance in Ferroelectric Composites", Solids 4(1):39–70. https://doi.org/10.3390/solids4010004
31. Tannhäuser K, Serrao PH, Kozinov S (2023) Three dimensional collocation-based mixed FE for flexoelectric solids. Comput Struct, accepted, in production
32. Mao S, Purohit PK, Aravas N (2016) Mixed finite-element formulations in piezoelectricity and flexoelectricity. Procee R Soc A Math Phys Eng Sci 472(2190):20150879. https://doi.org/10.1098/rspa.2015.0879
33. Nanthakumar SS, Zhuang X, Park HS, Rabczuk T (2017) Topology optimization of flexoelectric structures. J Mech Phys Solids 105:217–234. https://doi.org/10.1016/j.jmps.2017.05.010
34. Deng F, Deng Q, Shen S (2018) A three-dimensional mixed finite element for flexoelectricity. J Appl Mech 85(3):031009. https://doi.org/10.1115/1.4038919

35. Shu JY, King WE, Fleck NA (1999) Finite elements for materials with strain gradient effects. Int J Numer Meth Eng 44(3):373–391. https://doi.org/10.1002/(SICI)1097-0207(19990130)44:3<373::AID-NME508>3.0.CO;2-7

36. Amanatidou E, Aravas N (2002) Mixed finite element formulations of strain-gradient elasticity problems. Comput Methods Appl Mech Eng 191(15–16):1723–1751. https://doi.org/10.1016/S0045-7825(01)00353-X

37. Hu S, Shen S (2010) Variational principles and governing equations in nano-dielectrics with the flexoelectric effect. Sci China Phys Mech Astron 53(8):1497–1504. https://doi.org/10.1007/s11433-010-4039-5

38. Hu S, Shen S (2009) Electric field gradient theory with surface effect for nano-dielectrics. Comput Mater Continua (CMC) 13(1):26. https://doi.org/10.3970/cmc.2009.013.063

39. Çengel YA, Cimbala JM (2006) Fluid mechanics: fundamentals and applications. McGraw-Hill series in mech. engg. McGraw-Hill Higher Ed., Boston, Mass

40. Gao X-L, Park SK (2007) Variational formulation of a simplified strain gradient elasticity theory and its application to a pressurized thick-walled cylinder problem. Int J Solids Struct 44(22–23):7486–7499. https://doi.org/10.1016/j.ijsolstr.2007.04.022

41. Mao S, Purohit PK (2014) Insights into flexoelectric solids from strain-gradient elasticity. J Appl Mech 81(8):081004. https://doi.org/10.1115/1.4027451

42. Majdoub MS, Sharma P, Cagin T (2008) Enhanced size-dependent piezoelectricity and elasticity in nanostructures due to the flexoelectric effect. Phys Rev B 77(12):125424. https://doi.org/10.1103/PhysRevB.77.125424

43. El Gowini M, Moussa W (2009) A reduced three dimensional model for SAW sensors using finite element analysis. Sensors 9(12):9945–9964. https://doi.org/10.3390/s91209945

44. Zienkiewicz OC, Taylor RL (1997) The finite element patch test revisited a computer test for convergence, validation and error estimates. Comput Methods Appl Mech Eng 149(1–4):223–254. https://doi.org/10.1016/S0045-7825(97)00085-6